Research paper   **Open Access**

Synthesis, characterization and photocatalytic activity of visible-light-driven Mn_3O_4 and reduced graphene oxide- Mn_3O_4 nanocomposite

M.A. Mousa[(1)], M.M. Rashad[(2)], M.M. Mokhtar [(1)], Mahmoud E. El Shazli[(1)]

(1) Chemistry department, Faculty of Science, Benha University, Benha, Egypt.
(2) Electronic and Magnetic Materials Department, Advanced Materials Division,Central Metallurgical Research & Development Institute(CMRDI), Helwan, Cairo, Egypt.

ABSTRACT

Simple methods have been used to prepare rGO, Mn_3O_4 (M) and rGO-Mn_3O_4 (rGO-M) nanocomposite. The prepared samples were characterized by XRD, FT-IR, BET, TEM, , Photoluminescence (PL), and UV-vis absorption techniques. X-ray diffraction (XRD) and FT-IR confirmed the formation of rGO-M nanocomposites and transmission electron microscopy (TEM) study revealed that M nanomaterials with average size 75 nm were embedded on rGO surface. Under visible light illumination both M and rGO-M were successfully degrade the MB organic dye in water with more efficiency for the nanocomposite sample due to high surface area of rGO. The dye degradations were investigated under several experimental parameters such as pH, catalyst load, dye concentration, and catalyst recovery. The rGO-M nanocomposite sample showed good photostability after five cycling process. A photocatalytic mechanism has been propsed for the photodegradation process.

1. Introduction

Graphene, a single two dimensional (2D) sp^2 hybridized carbon network [1, 2] has drawn significant consideration owing to extraordinary specific surface area (2630 m^2 g^{-1}), excellent high electrical conductivity (~5000 W m^{-1} K^{-1}) and electron mobility (200,000 cm2 V^{-1} s^{-1}) [3]. Furthermore, reduced graphene oxide (rGO) [4] fixes a high degree of the sp2 bonded structure to grapheme, it develops a conductive 2D carbon material that can move charges between the active nanostructured materials [5].

Nowdays, graphene-based nanocomposites are a new class of nanomaterials with countless potential for removing wastewater pollutants [6]. A variety of metal and metal oxide nanoparticles can be attached to graphene materials, to create effective sorbents or catalysts[7]. These graphene-based nanocomposites frequently display enhanced sorptive, catalytic or photocatalytic operation, compared with the respective bare metal oxide nanoparticles [7,8]. A number of reports have been dedicated to understand the mechanisms in which reduced rG) enhances the performance of graphene-based nanocomposites in contaminant removal [7-10]. It is important to note that rGO contain substantial amounts of epoxy, phenolic, carbonyl, and carboxyl groups. These surface O-functionalities may participate directly in redox reactions.

Here, in this work, we used the hydrothermal method for synthesizing Mn_3O_4 nanoparticles and rGO-M nanocomposites and evaluating their photocatalytic efficiency using aqueous solution of MB under visible light irradiation. The as-synthesized materials has been characterized by XRD, FTIR, BET, TEM, photolumiscence and UV-vis reflectance spectroscopy. A photocatalytic mechanism has been suggested.

2. Experimental

2.1. Materials

Graphite (99.995%) was purchased from Fluka Switzerland, hydrazine monohydrate (NH_2-NH_2.H_2O) 99%, potassium permanganate ($KMnO_4$) 97%, sodium nitrate ($NaNO_3$) 95%, hydrogen peroxide (H_2O_2) 30%, ethanol (C_2H_5OH) 99%, sulphuric acid (H_2SO_4) (98%) was purchased from Adwic pharmaceutical and chemicals company Egypt. Methylene blue (MB) dye (99.95%), NaOH and HCl were purchased from Sigma-Aldrich.

2.2. Catalyst fabrication

2.2.1. Preparation of GO

Graphene oxide (GO) was synthesized from natural graphite according to a modification of the Hummers–Offerman method [11]. In brief, graphite powder (5 g) was dispersed in cold concentrated sulphuric acid (H_2SO_4, 115 mL, 98 wt%, in a dry ice bath). This is followed by adding 2.5 g of $NaNO_3$ into the solution and then 15 g) of $KMnO_4$ was slowly added with continuous strong stirring for two hours at temperatures below 10°C, followed by one hour at 35°C. Then, 250 ml of de-ionized water was inserted into the reaction in an ice bath. When the effervescence ended, we increased the temperature of the reaction to 98°C and kept for 10 min before cooling it to room temperature. Following, 50 ml of H_2O_2 was added to the solution and heating to 90°C and kept for 30 min. The produced mixture was centrifuged

and washed several times with boiling water until the pH of the supernatant turns out to be neutral. Lastly, the produced solid was dried at 60°C for 24 h.

2.2.2. Reduction of GO

0.1 gram of the previously prepared graphene oxide (GO) was first dispersed in 30 ml de-ionized water and sonicated for 30 min, following by heating to 100°C with adding 3 ml hydrazine hydrate and keeping at 100 °C for 24 h. The reduced graphene oxide was then gathered by filtration and washed using distilled water several times to remove the excessive hydrazine. The final product was stored by vacuum filtration and dried at 80°C and denoted as rGO.

2.2.3. Preparation of Mn_3O_4

Mn_3O_4 prepared by the addition of 0.02 mol $KMnO_4$ to 100 ml distilled water followed by adding 20 ml ethylene glycol with magnetically stirring for 1 h at room temperature. The suspension was then transferred to a 125-mL-capacity Teflon-lined autoclave and heated under autogenous pressure to 120 °C for 4 h. The autoclave was then allowed to cool to room temperature. Finally, the precipitate obtained was washed with excess water and dried and denoted as M.

2.2.4. Synthesis of rGO-M

The rGO/Mn_3O_4 composites synthesized by hydrothermal method via dispersing 0.222 g rGO by sonication in 100 ml of distilled water for 1 h. Then, adding 0.02 mol $KMnO_4$ to the suspension, followed by 20 ml of ethylene glycol and magnetically stirring for one hour at room temperature. The suspension was then relocated to a 125-ml Teflon-lined autoclave and heated to 120 °C for four hours. Finally, the autoclave was cooled to room temperature. The precipitate obtained was washed several times with bi-distilled water and dried and denoted as rGO-M.

2.2.5. Reused rGO-M catalyst:

We start the recyclability test by large amount from catalyst in first cycle, then separate it by centrifuge and drying by air and reuse the same catalyst again, and repeat it with every cycle.

2.3. Characterizations:

2.3.1. X-ray diffraction

X-ray diffraction (XRD) was measured at room temperature by using a Philips diffractometer using Model PW-3710. The patterns were progressed with Ni-filtered copper radiation (λ = 1.5418°A) at 30 kV and 10 mA with a scanning speed of 2θ = 5°/min. The mean crystallites size were calculated using the Debye–Scherrer Eq. (1),in which K is a constant equal 0.9, λ is the wave length of the Cu Kα radiation, β is the half peak width of the diffraction peak in radiant. The different phases were recognized with the help of ASTM powder data files.

$$D = \frac{K\lambda}{\beta \cos\theta} \qquad \text{Eq. (1)}$$

2.3.2. FTIR spectroscopy

The Fourier transform infrared (FT-IR) spectra were monitored via a single beam Thermo scientific Nicolet iS10 instrument. The samples were grounded with KBr (1:100) to form tablets, and thus confined into the sample holder in the spectrometer cavity to record the measurements in the 4000-400 cm^{-1} region.

2.3.3. Brunauer–Emmett–Teller technique (BET)

The surface texturing properties were determined by using N_2 adsorption isotherms technique measured at 77 K by a conventional volumetric apparatus; (Quantachrome NOVA automated). The pore size distribution was decided from the desorption branch of isotherm using BJH analysis.

2.3.4. Ultraviolet-visible diffuse reflectance spectroscopy

Diffuse reflectance ultraviolet-visible spectroscopy (UV–vis DRS) of the studied samples were performed at room temperature using a JASCO V-570 spectrophotometer in the range of 200–800 nm with employing $BaSO_4$ as the reflectance standard.

2.3.5. Transmission electron microscope (TEM)

TEM micrographs were measured using a JEM-2100 model which achieves high resolution of 0.19 nm at a power of 200 kV. The powder samples were put on carbon foil with a microgrid. TEM images were observed with minimum electron irradiation to prevent damaging of the samples structure. Selected area electron diffraction (SAED) images were also recorded at an accelerating voltage of 200 kV.

2.3.6. Photoluminescence spectroscopy

The photoluminescence (PL) excitation and emission spectra were measured on a thermo scientific fluorescence spectrophotometer model Lumina. The measurements were conducted at room temperature using a He/Cd laser (310 nm) as an excitation source.

2.3.7. Raman spectroscopy

Raman spectra were measured with SENTERRA II Raman spectrometer manufactured by BRUKER using 785-532 nm with multi-laser excitation. It covered a full Raman spectrum in a single scan with 4 cm^{-1} resolutions.

2.4. Photocatalytic reaction

A high-pressure Hg lamp of 160 W with a special UV cut-off filter (λ > 420 nm) presenting visible light source; with an average light intensity of 40 $mWcm^{-2}$, was used in the photocatalytic measurements. The photocatalyst was suspended in 100 ml of a definite aqueous concentration of methylene blue (MB). Firstly, the reacted solution was stirred in the dark for 60 min to guarantee the organization of an adsorption-desorption equilibrium. During the irradiation process, 2 ml aliquots were eliminated at definite time intervals and analyzed with a JASCO V-630 spectrophotometer.

For discovering the reactive species might be created in the photocatalytic reaction, various scavengers comprising isopropanol IPA (a quencher of $\cdot OH^-$), p-benzoquinone (a quencher of $\cdot O^{2-}$), triethanolamine TEOA (a quencher of h^+), and carbon tetrachloride (a quencher of e^-) at a concentration of 1.0 mM were used.

3. Results and discussions

3.1. Structural and morphology study

The XRD of the investigated samples is shown in Fig. (1). In the case of a single system: the pattern of the reduced

graphene oxide (rGO) Fig. (4-1.a), shows wide reflections at ~ 24° and 42° (equivalent to d spaces of 0.37 and 0.21 nm), signifying restacking to create a defectively ordered graphite-like material. The obtained spectrum differs than that characterized for GO with $2\theta=11.9°$ (d (002) =7.63 °A) [12], which confirms the frormation of rGO. The XRD of Mn_3O_4 (M) powdered sample, Fig. (4-1.c), show peaks at 17.91°, 28.73°, 32.29°, 36.02°, 44.42°, 50.65°, 58.42°, 59.81° and 64.55° corresponding to (101), (112), (103), (211), (220), (105), (321), (400) and (224) planes characterized for

Hausmannite tetragonal Mn_3O_4 (JCPDS 24-0734) with the space group I41/amd (JCPDS 24-0734, a = b =5.762 Å, c = 9.47 Å. The absence of any impurity peaks, demonstrating the purity of the Mn_3O_4 and the fine sharp peaks verified that the prepared Mn_3O_4 particles are well crystallized. The XRD pattern of rGO-M nanocomposites was similar to the Mn_3O_4 nanoparticles except for a broad peak at ca. 23.2°, which corresponded to rGO with the interplanar spacing of 0.328 nm [12].
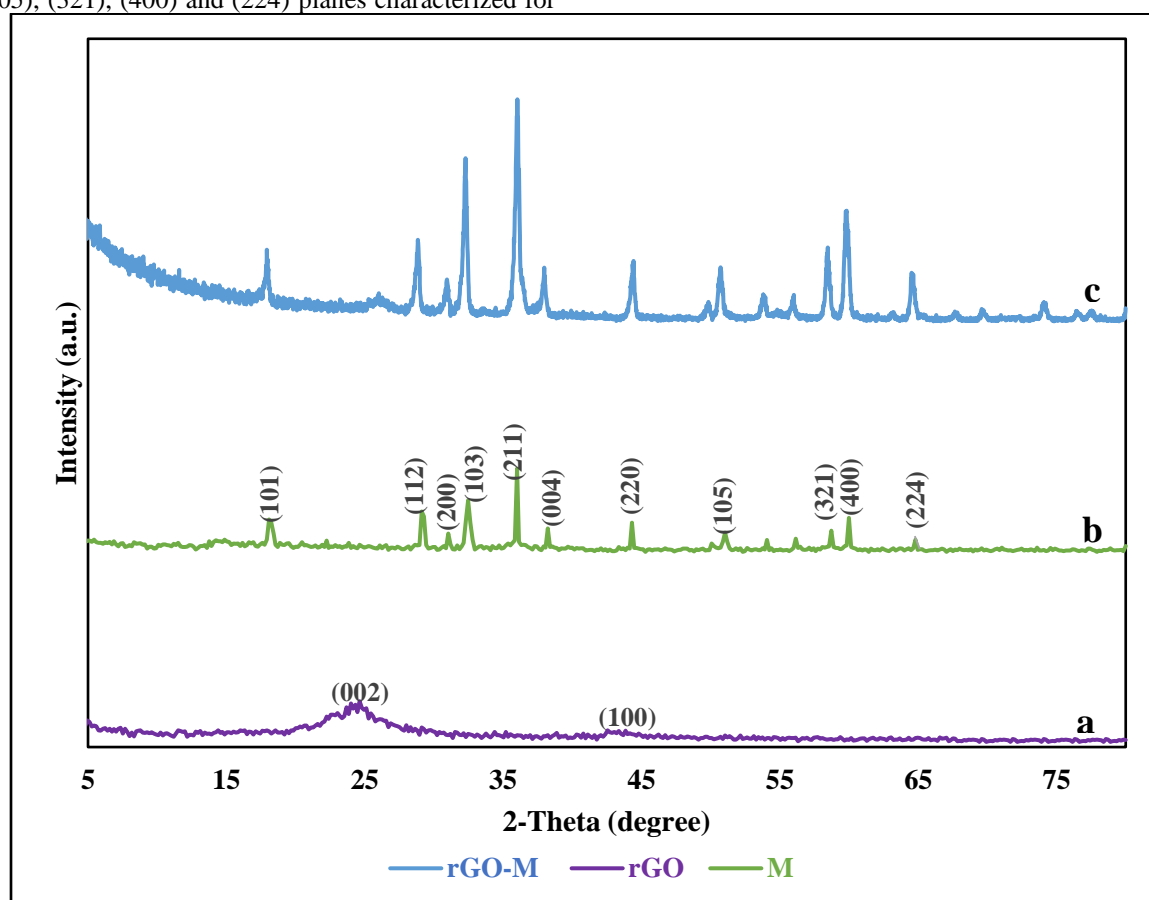

Fig. (1): XRD patterns of rGO, (a); Mn_3O_4, (b) and rGO-M (c).

Fig. (2) represents the FT-IR spectra of the investigated samples in the range of 4000–400 cm^{-1}. The FT-IR spectrum of rGO presented in Fig. (2) show the stretching and bending of a hydroxyl group at 3420 and 1620 cm^{-1}, respectively, C=O carbonyl stretching at 1728 cm^{-1}, and C–O epoxide group stretching at 1023 cm^{-1} [13]. As well as bands at 1376 and 1023 cm^{-1}, which are attributed to the stretching vibrations of C–OH and C–O vibrations from alkoxy groups, respectively [14-15].The band appears at 1083 cm^{-1} is assigned to in-plane bending mode of C-H. The peak observed at 1580 cm^{-1} is attributed to the phenol C=C ring stretching.

The FT-IR spectrum of Mn_3O_4 sample (shown in Fig. (2)) displays three major absorption bands in the range of 400–650 cm^{-1}. The band located at 624 cm^{-1} is assigned to Mn–O

stretching vibration modes in tetrahedral sites, whereas the band located at 511 cm^{-1} matches to the distortion vibration of Mn–O in an octahedral environment. The third vibration band, located at 412 cm^{-1}, is assigned to the $Mn^{3+}-O$ vibration in the octahedral site of Mn_3O_4 [16-19]. The FT-IR spectrum of Mn_3O_4 also shows a broadband at 3430 cm^{-1} besides a narrow one at 1617 cm^{-1} corresponding to the O–H vibrating mode of the adsorbed water.

For binary systems, the spectrum of rGO-M, Fig. (2) shows almost the disappearance of C-O absorption bands, and a decrease in the intensity of absorption peaks of O-H. This suggests the formation of a weak interaction in Mn–O–C [20]. Furthermore, the intensity of the tetrahedral and octahedral bands present in the spectrum of Mn_3O_4 in the range of 400–650 are slightly shifted. This refers to a

presence of a strong interaction between the moieties forming the sample. Moreover, shifting the Mn–O vibrations in the composite sample compared to the bare Mn_3O_4 reveals to the strong interaction existing between rGO and Mn_3O_4. It can be also seen that the band area ratio of tetrahedral/octahedral in the binary system is higher than that in the pure Mn_3O_4 sample.
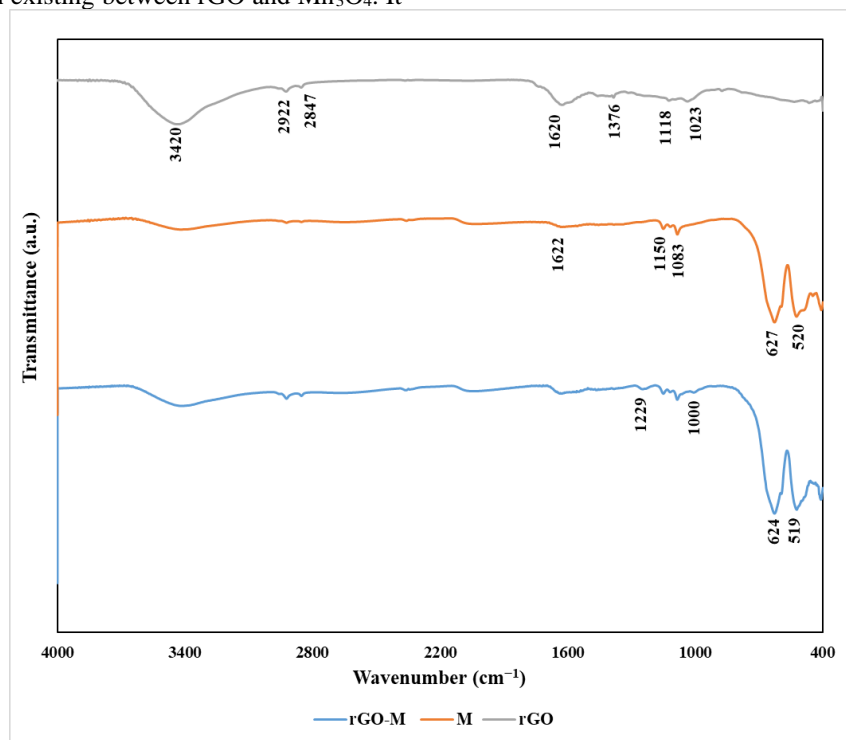

Fig. (2): FT-IR of rGO, M and rGO-M.

Fig. (3) shows the nitrogen adsorption-desorption isotherms and the pore size distributions of investigated specimens. Corresponding to IUPAC [21-23] adsorption isotherms system, all the specimens demonstrated V type isotherms, which pointed to that the specimens could make restricted multilayer adsorption. Table 1 summarizes the BET surface areas, S_{BET}, total pore volumes, and average pore sizes of the synthesized materials.

Type H3 adsorption isotherm is detected for rGO (shown in Fig. (3)), demonstrating that the sample is a mesoporous material. The apparent hysteresis loop can be watched at relative pressures ranged from ~ 0.47 to 1.0. The pore size distribution curve (given in Fig. (3)) determined by the Barret-Joyner-Halenda (BJH) method shows that the pore sized is ranged between 2 to 50 nm with a most probable pore diameter of 8.1 nm. The S_{BET} is calculated to be 309.9 $m^2 g^{-1}$.

Fig. (3) illustrates the N_2 adsorption/desorption isotherms of Mn_3O_4. It demonstrates a capillary condensation step at relative pressure ranged between ≈0.85–0.98, which could be specified by a hysteretic loop. This behavior generally happened in Meso-porous adsorption. The hysteretic loop is appropriate to H3 type according to IUPAC isotherms system, which revealed that the adsorption presented unrestricted adsorption volume at relatively high pressure and the adsorption volume rose with pressure increasing. This category of hysteretic loop frequently appeared in materials which hold long, narrow porous structure. The BET surface area of the sample is 14.4 m^2/g which is much higher than the commercial Mn_3O_4 crystals (1 m^2/g), and the pore distribution lies in the range of 1-5 nm with a maximum at 1.5 nm.

The results obtained show that the specific surface area of the studied samples increases in the order:

$$rGO > rGO-M > Mn_3O_4(M)$$

Whereas the pore size diameter increases according to:

$$rGO > rGO-M > Mn_3O_4$$

Table (1): Surface parameters of prepared samples:

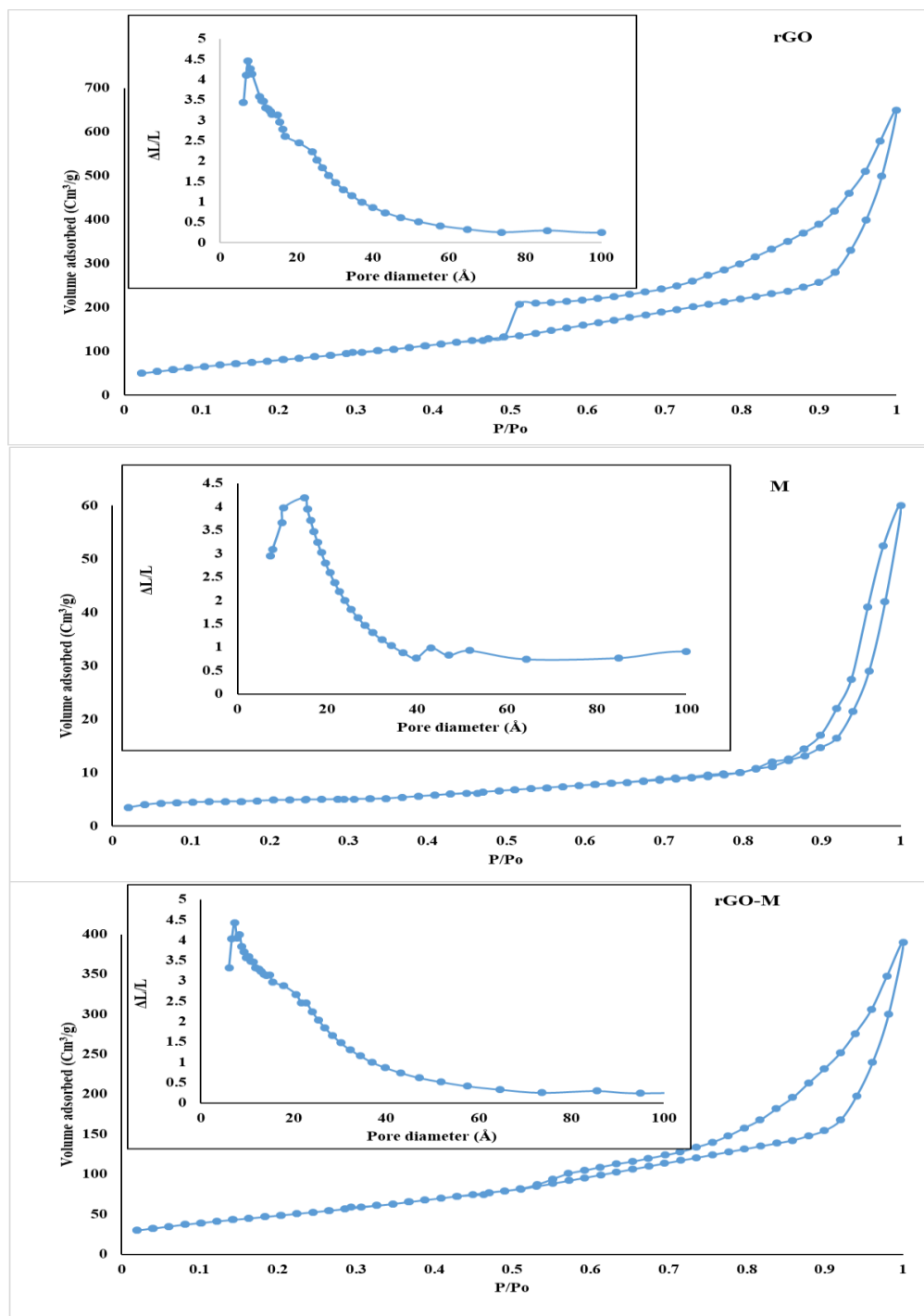| System	rGO	M	rGO-M
S_{BET} (m^2/g)	309.9	14.4	185.9
r(A)	8.1	1.5	7.5

Fig. (3): N2 adsorption-desorption isotherms of rGO, M and rGO-M.

The Transmission electron microscopy (TEM) images of rGO and rGO-M samples are presented in Fig. (4). The image of the as-prepared rGO, Fig. (4.a), shows fibers with a diameter of 10 nm. TEM image of rGO-M indicates that the Mn_3O_4 particles are covered and decorated with rGO fibers. The Mn_3O_4 NPs can be easily distinguished based on the differences in their size and contrast. The average size of Mn_3O_4 NPs is estimated to be ca. 75 nm.
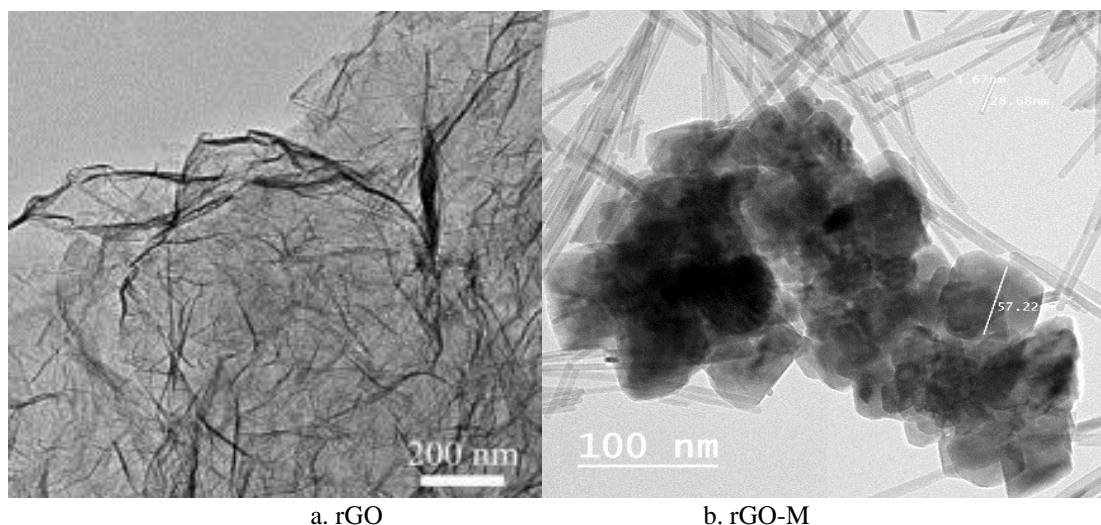
a. rGO   b. rGO-M
Fig. (4): TEM images of (a.) rGO; and (b.) rGO-M.

3.2. Optical properties and UV-Vis study

Photoluminescence (PL) spectroscopy studies can provide important knowledge about the efficiency of charge carrier trapping and recombination in semiconductor particles. Fig. (5) shows the PL spectra for all the investigated samples. The PL spectrum of rGO shows small emission peak at ca. 365 nm besides a large peak at about 680 nm originated from the optical transitions from structural disorder-induced localized states in the p-p* gap of sp^2 [24].

The PL emission spectrum of as-synthesized Mn_3O_4 nanostructures displays, four obvious PL emission peaks at 390, 490, 590 and 690 nm. The highest emission peak yellow band centered at 590 nm. The UV emission band located at 390 nm corresponds to the recombination and emission of free excitons through an exciton-exciton collision process near the band edges of Mn_3O_4 crystals [25]. A prominent blue emission at 490 nm can be assigned to the radial recombination of the photo-generated hole with an electron resulting in singly ionized oxygen vacancy-related defects. The yellow PL emission located at 590 nm can be attributed to the d–d transitions involving Mn^{3+} ions [26].

PL emission of rGO-M represented in Fig. (5) shows a decrease in the intensities of the observed peaks in PL of the bare Mn_3O_4 besides peaks at 465, 550 and 735 nm, which may be attributed to the rGO moieties. The decrease in intensity of the peaks corresponding to Mn_3O_4 reveals to the lower recombination rates of electrons and holes under light irradiation.

Fig. (6) shows UV-visible diffuse reflectance spectra of the investigated samples. The spectra of the rGO-M, and Mn_3O_4 samples are different. The diffuse reflectance spectra (R) obtained were changed to Kubelka-Munk function data F(R) using equation (2), which allows the optical absorbance of a sample to be approximated from its reflectance [27].

$$F(R) = (1-R)^2 / 2R \qquad \text{Eq. (2)}$$

The reflectance (f (R)), which is proportional to the absorption coefficient [28] is represented for each one of the investigated samples in Fig. (7).

The UV visible absorption spectra of the samples containing Mn_3O_4 produces from two types of transitions corresponding to Mn^{2+} ions and Mn^{3+} ions.

The obtained optical absorption data of the studied samples were used to estimate their band gap energy, E_g, by using Tauc's relationship [29] in Eq. (3):

$$[F(R) h\nu]^n = A(h\nu - E_g) \qquad \text{Eq. (3)}$$

where h is Planck's constant, ν is the frequency of vibration, $h\nu$ is the photon energy, A is a proportional constant, and exponent n has values depending on the nature of electronic transition which assumes the values 1/2, 3/2, 2, and 3. From the plots of $[F(R)h\nu]^n$ vs photon energy ($h\nu$) (shown inFig. (7)) the best fitting was found for direct band gap transition with n=1/2. From the intercepts of the tangents with the energy axis ($h\nu$) E_g values were determined and found to be 1.35, 1.97 eV and 1.92 eV for rGO, M and rGO-M, respectively.
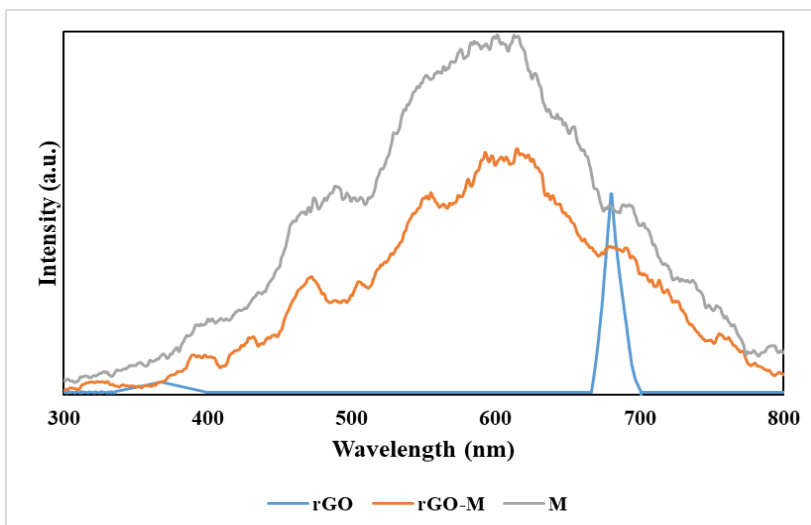
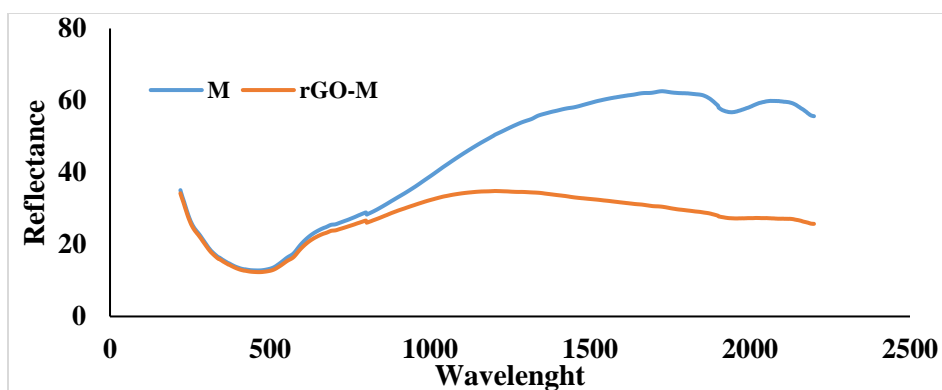Fig. (5): Photoluminescence of rGO, M and rGO-M.

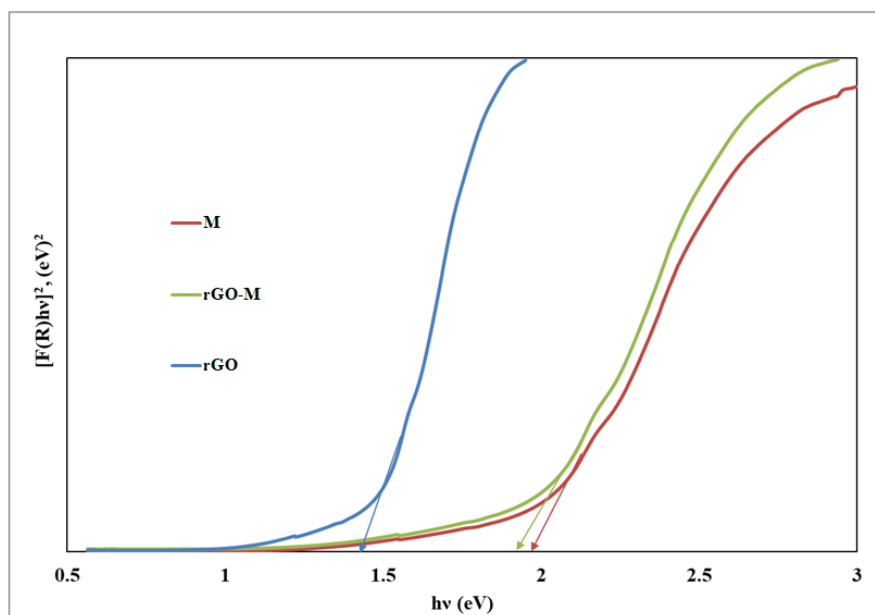Fig. (6): UV−vis reflectance spectra of M and rGO-M.

Fig. (7): Tauc plots of $[f(R)hv]^n$ vs photon energy (hv).

3.3. Photocatalyst study:

For study the photocatalytic capabilities of the as-synthesized nanomaterials (rGO, M and rGO-M). Definite weight of catalyst (1 g.L^{-1}) were initially left for 60 min in10 ppm methylene blue (MB) solution before irradiation to reach equilibrium adsorption, followed by exposure to the visible light irradiation ($\lambda > 420$ nm, power = 160 W) for 240 min at room temperature.

The reduced graphene oxide sample showed 100 % adsorption of methylene blue in dark before exposure to the visible light, whereas M and rGO-M samples showed photodegradation of 21 % and 100 % after 240 min illumination, as shown in Fig. (8).
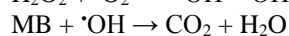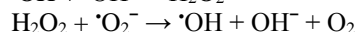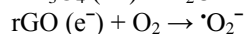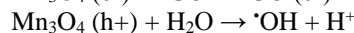
The diverse activity levels of the photocatalysts obviously demonstrate that the photocatalytic activity is strongly depended on the composition of the photocatalysts, and rGO-M sample exhibits the higher photocatalytic activity under visible light illumination than pure Mn_3O_4 sample. This goes in a parallel way with the high BET surface area and pore diameter as well as lower gap energy of rGO-M comparable with pure Mn_3O_4 sample. Plotting ln C_o/C vs. time showed straight lines (see Fig. 8.b.) with slopes indicative to the pseudo first order rate constant for the photocatalytic reaction.

The rate constant values are found to be 1.22×10^{-2} and 9.0×10^{-4} min^{-1} at 298 K for rGO-M   and Mn_3O_4, respectively. Since, the nanocomposite rGO-M sample presented the most promising photoactivity result, it has been used for performing further reactions.

The lowly photocatalytic performance of the virgin Mn_3O_4 nanoparticles is due to the aggregation of Mn_3O_4 nanoparticles which leads to the formation of larger sized particles and decrease of the surface area, as shown in our results (1.5 m^2/g^2) and reported in the literature [30]. Interestingly, a high photodegradation of MB was observed when a photocatalyst of Mn_3O_4 nanoparticles combined with reduced graphene oxide sheets. The enhanced catalytic activity of the nanocomposites over MB dye degradation is due to having benzene or phenyl ring-like structure of the graphene and as well as MB molecules [31, 32]. Because MB molecules are positively charged in nature and rGO surface has oxygenated groups, thus MB molecules get adsorbed onto the surface of rGO via $\pi-\pi$ stacking interaction. This in turn provides a greater amount of MB concentration near the Mn_3O_4 nanoparticles on the surface of rGO and therefore leading to the more efficient contact between them. The rGO is a 2D material and has a large surface area which results in superior electrical conductivity as well as unique transport properties, making it a great electron-transport material in the process of photocatalysis.

For a traditional semiconductor photocatalyst, both electrons and holes generated in the photocatalyst could decompose pollutants directly. The highest photocatalytic degradation efficiency of rGO-M nanocomposite can be explained as follows: when the Mn_3O_4 nanoparticles are excited with photon energy higher than the band gap of Mn_3O_4, the electrons in the valence band (VB) move to the conduction band (CB) generating equal amounts of holes in VB. The photo-generated electrons are transferred from the CB of Mn_3O_4 to the rGO where rGO acts as a good electronic acceptor and transferor; therefore, the electrons finally travel towards the MB dye due to the good interaction between rGO and MB molecules. Thus, the lifetime of the excited electrons (e$^-$) and holes (h$^+$) is prolonged in the transfer process. Finally, Mn_3O_4 (h$^+$) can oxidize H_2O or OH$^-$ toward $^\bullet$OH and hydrogen peroxide (H_2O_2) will be formed by the reaction between $^\bullet$OH and other $^\bullet$OH. On the other hand, rGO (e$^-$) can be trapped by the dissolved O_2 to form superoxide radical anions ($^\bullet O_2^-$). The interaction of $^\bullet O_2^-$ and H_2O_2 results in the formation of $^\bullet$OH which is the main species for the degradation of dye molecules. The following equations illustrate this mechanism:

$$Mn_3O_4 + h\upsilon \rightarrow Mn_3O_4 \, (e^-) + Mn_3O_4 \, (h^+)$$
$$Mn_3O_4 \, (e^-) + rGO \rightarrow rGO \, (e^-)$$
$$Mn_3O_4 \, (h+) + H_2O \rightarrow {}^\bullet OH + H^+$$
$$rGO \, (e^-) + O_2 \rightarrow {}^\bullet O_2^-$$
$${}^\bullet OH + {}^\bullet OH \rightarrow H_2O_2$$
$$H_2O_2 + {}^\bullet O_2^- \rightarrow {}^\bullet OH + OH^- + O_2$$
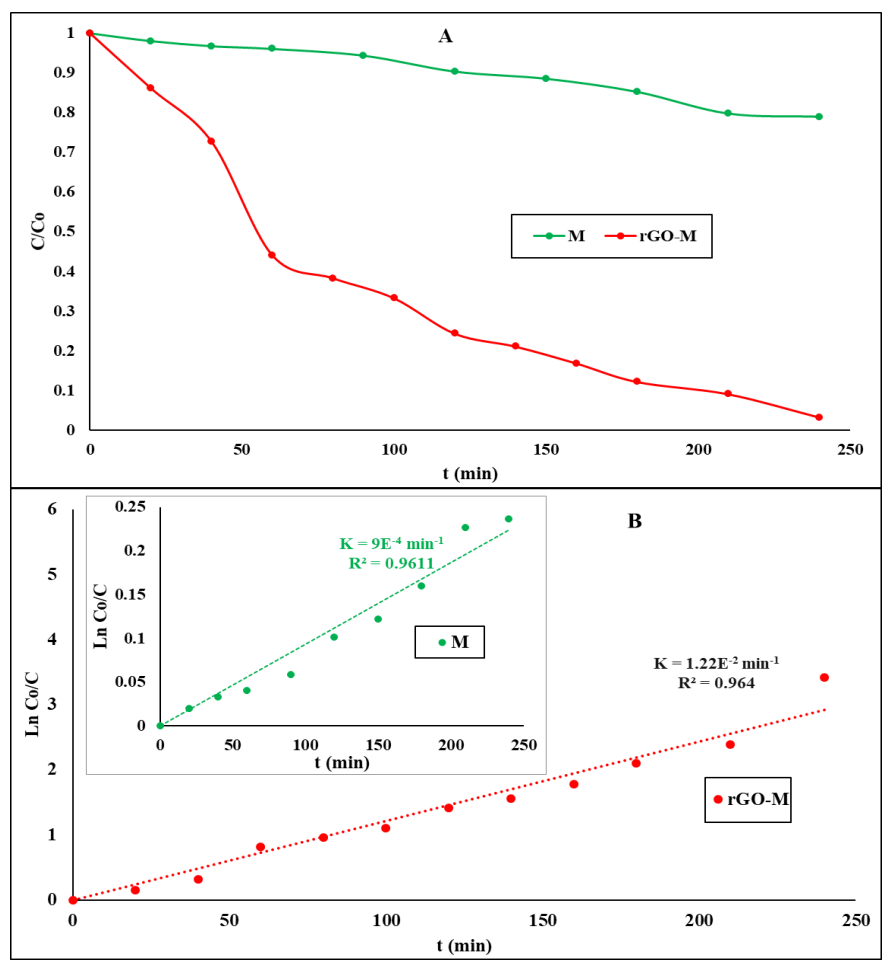$$MB + {}^\bullet OH \rightarrow CO_2 + H_2O$$

Fig. (8): A. Photocatalytic degradation of the MB dye by M and rGO-M photocatalysts under visible light irradiation: reaction conditions: (lamp power 160 W, filter λ= 420 nm, catalyst weight 1 gL^{-1}, dye conc. 10 ppm). B. The kinetic fits for the same reactions.

3.3.1. Effect of pH of dye solution

The photocatalytic degradation of organic material is actually comprised with a sequence of reactive species as found with the photo-induced charges (e$^-$ and h$^+$) such as $^{\bullet}$OH or $^{\bullet}$O$_2{}^-$, which are mainly concerned in the photocatalytic degradation progression [33]. Moreover, the effect of solution pH is a significant factor in the degradation of contaminants because it transactions the mechanism included at the photocatalyst surface. The catalytic procedure is significantly motivated with the sorption of contaminants onto the catalyst surface and sorption is greatly reliant on the solution pH. Really, the size of the catalyst aggregates, the charge of the surface, as well as the locations of valence and conduction bands are affected by solution pH [34]. Thus a pH reliance photodegradation of the MB is performed at pH ranged from pH ~4.0 to 11.0 in the presence of rGO-M catalyst. Further, the percent degradation of MB is evaluated and the outcomes obtained are illustrated graphically in Fig. (9). Results are gotten at the achievement of 200 min of irradiation. The optimum pH for the degradation in dark was found to be 11 and this can be explained on the basis of adsorption process rather than photocatalytic behavior. But the photocatalytic behavior was found to be higher in acidic medium at pH less than 7. These results are illustrated in Table (2) and Fig. (9).

Table (2): The rate of reaction of MB photodegradation at different pH values via rGO-M photocatalyst, under visible light, and under the mentioned reaction conditions:

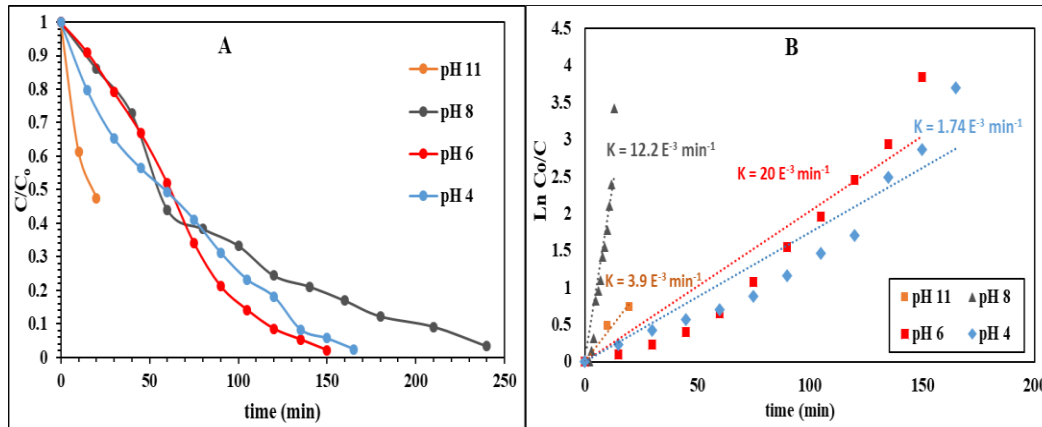| Reduced organic matter	Catalyst weight	Catalyst used	pH	Specific rate constant k x 10^3 (min^{-1})
10 ppm Methylene blue	1 g/L	rGO-M	4	1.74
			6	20
			8	12.2
			11	39

Fig. (8): A. Effect of change Fig. (9): Effect of pH on the degradation activity of the rGO-M photocatalyst towards MB under Vis. light illumination, reaction conditions: (lamp power= 160 W, filter λ=420 nm, catalyst load 0.5 g/L, 1.0 g/L and 2.0 g/L dye conc. 10 ppm). B. The kinetic fits for the same reactions.

3.3.2. Effect of Catalyst dose

The impact of catalyst dosage of rGO-M on the MB removal was also studied and the results are shown in Fig. (10) and Table (3) for initial dye concentration 10 ppm and pH ~7. The percentage degradation was found to increase with increasing the dosage of the catalyst. The rise in catalyst amounts spreads the number of active sites on the photocatalyst surface, which consequently enhance the number of hydroxyl ($^{•}OH$) and superoxide ($^{•}O_2$) radicals.

Table (3): The rate of reaction of MB photodegradation by using different catalyst weight from MG:

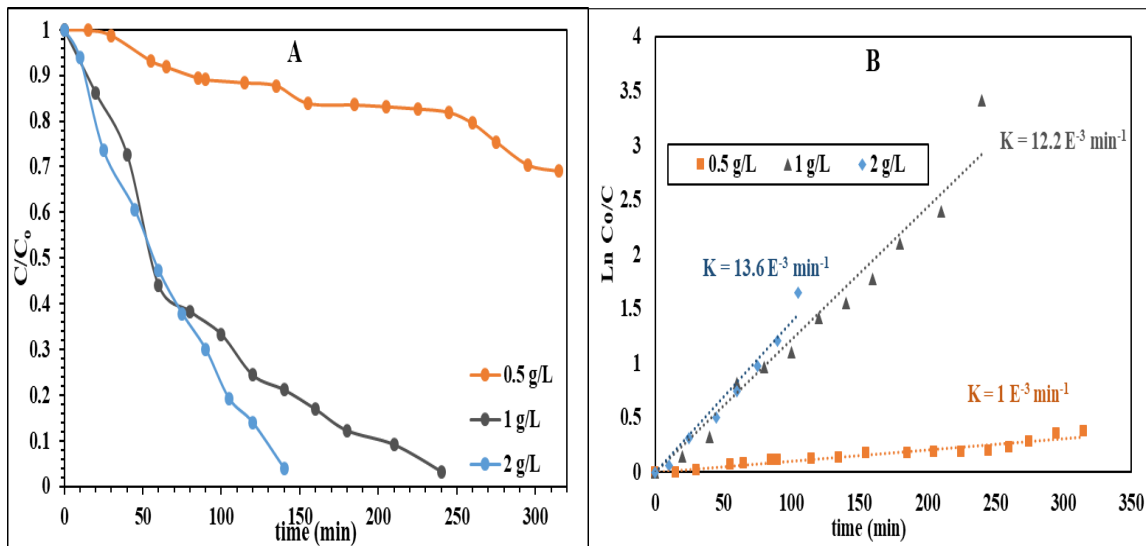| Reduced organic matter	Catalyst weight	Catalyst used	Specific rate constant $k \times 10^3$ (min^{-1})
10 ppm Methylene blue	0.5 g/L	rGO-M	1
	1 g/L		12.2
	2 g/L		13.6

Fig. (10): (A) Effect of catalyst weight on the degradation activity of the rGO-M photocatalyst towards MB under Vis. light illumination: reaction conditions: (lamp power= 160 W, filter λ=420 nm, catalyst load 0.5 g/L, 1.0 g/L and 2.0 g/L dye conc. 10 ppm);(B) The kinetic fits for the same reactions.

3.3.3. Effect of initial dye concentration:

The effect of MB dye concentration in the range of 5-20 ppm on its photocatalytic degradation over rGO-M catalyst has been investigated. It is known that the percentage of total removal of the dye decline by increasing its concentration. This is because the effective contact probabilities between the dye molecules and the catalyst are enlarged at lower dye concentrations, on the other hand, the percent source of active species are much reduced at higher dye concentration. In our study, we found this rule, as shown in Fig. (11) and table (4).

Table (4): The change in reaction rate with change in concentration of MB.

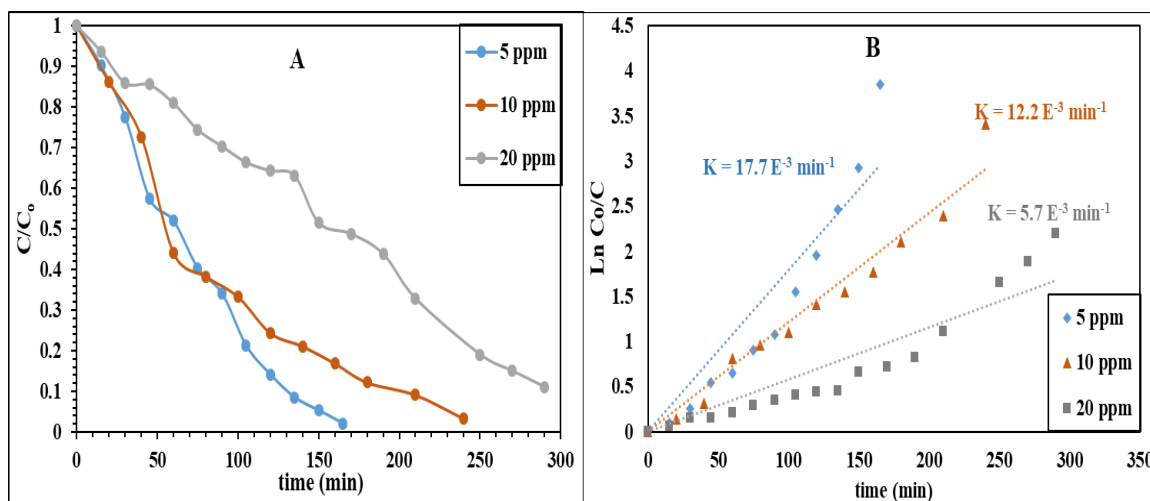| Catalyst used	Catalyst weight	Reduced organic matter	Specific rate constant $K \times 10^3$ (min^{-1})
rGO-M	1 g/L	5 ppm MB	17.7
		10 ppm MB	12.2
		20 ppm MB	5.7

Fig. (11): (A)The degradation activity of the rGO-M photocatalyst towards MB with different concentrations under Vis. light illumination: reaction conditions: (lamp power= 160 W, filter λ=420 nm, catalyst load 1.0 g/L, dye conc. 10 ppm); (B). The kinetic fits for the same reactions.

3.3.4. Proposed Photocatalytic Degradation Mechanism

To determine the possible degradation mechanism of MB dye on the rGO-M photocatalyst, different scavengers were introduced to quench the relevant active species. The effect of the addition of 2 ml from 1mmol of benzoquinone (PBQ) , isopropanol (IPA), triethanolamine (TEOA), and carbon tetrachloride (CCl$_4$), as $^{\bullet}O_2^{-}$, $^{\bullet}OH$, hole, electron scavenger, respectively, on the photocatalytic oxidation of 50 ml MB dye (10 ppm) in presence of rGO-M was studied. The results obtained are illustrated in Fig. (12) and summarized in Table (5). The figure shows a decrease in the degradation rate according to the order CCl$_4$ > TEOA > IPA > PBQ. This reflects the small effect of the $^{\bullet}O_2^{-}$ species than that $^{\bullet}OH$ in the degradation process. Whereas the significant decrease in the degradation rate of MB in presence of TEOA and CCl$_4$ reflects the effectiveness of both electrons (e^{-}) and positive holes (h^{+}) in the MB oxidation mechanism.
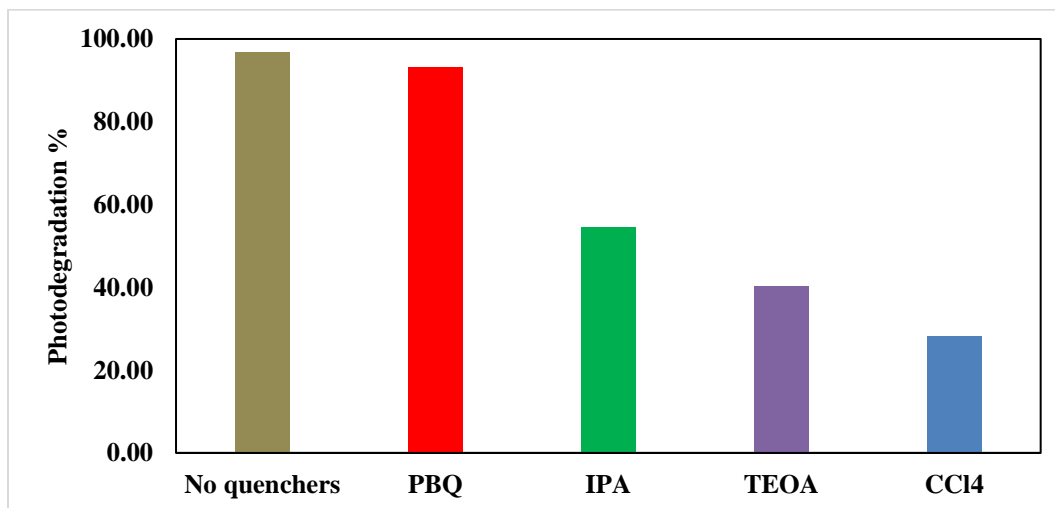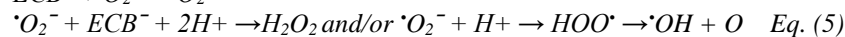

Fig. (12): Effect of reactive scavengers on the degradation activity of the rGO-M nanocomposite towards MB under Visible light and reaction conditions: (lamp power= 160 W, filter λ=420 nm, catalyst load 1.0 g/L, dye conc. 10 ppm).

On the basis of the results obtained, we can suggest a mechanism illustrated in equations from Eq. (4 to 8) In the rGO-M photocatalyst, M connected with the surface of rGO creates (e^-)- (h^+) pairs when exposed to visible light irradiation. Valuable separation of the charges is reached when the electrons absorbed by rGO react with the adsorbed O_2 to yield $^\bullet O_2^-$ which in turn transferred into $^\bullet OH$; together with OH^- offered to produce $^\bullet OH$ as well. At the same time, the photo-generated h^+ could be captured by each of oxygen in the M lattice as well as present on rGO sheets to form the $^\bullet OH$ active species. Moreover, the photogenerated positive hole (h^+) in the VB is also responsible for producing $^\bullet OH$ through the reaction with H_2O.

$$ECB^- + O_2 \rightarrow {}^\bullet O_2^- \qquad\qquad Eq.\ (4)$$

$${}^\bullet O_2^- + ECB^- + 2H+ \rightarrow H_2O_2\ and/or\ {}^\bullet O_2^- + H+ \rightarrow HOO^\bullet \rightarrow {}^\bullet OH + O \quad Eq.\ (5)$$

$${}^\bullet O_2^- + H_2O_2 \rightarrow {}^\bullet OH + OH^- + O_2 \qquad\qquad Eq.\ (6)$$

$$H_2O_2 + h^+ \rightarrow 2{}^\bullet OH \qquad\qquad Eq.\ (7)$$

$$OH^- \rightarrow {}^\bullet OH + e^- \qquad\qquad Eq.\ (8)$$

Table (5): Show rate constant and R^2(square correlation factor) with and without addition of PBQ, IPA, TEOA and CCl_4

System	Reaction rate constant, $K \times 10^3\ min^{-1}$	R^2
No quenchers	12.2	0.96
PBQ	10.6	0.99
IPA	3.50	0.98
TEOA	2.50	0.99
CCl_4	1.70	0.98

3.3.5. Recyclability of rGO-M catalyst

The stability of the photocatalytic materials is of great importance if they are to be practically applicable. The prepared rGO-M nanocomposite is separated for reuse from the MB solution by using method reported in the experimental section. Fig. (13) and Table (6) show the recycling results of the rGO-M nanocomposite for MB degradation under visible light illumination. After three recycles of the photocatalytic degradation of MB, the catalytic activities of the rGO-M composite showed just a slight decrease.
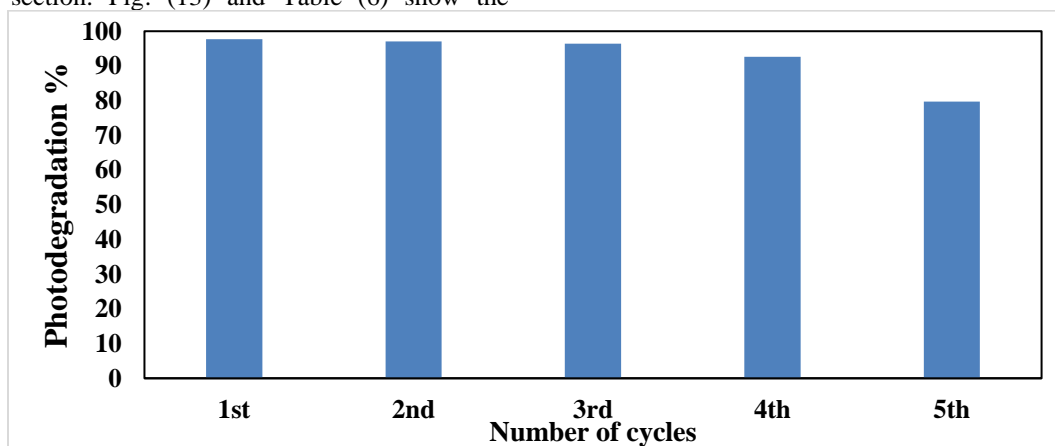

Fig. (13): Recycle test during degradation of MB using rGO-M as a photocatalyst under Vis. illumination.

Table (6): summaries the rate of reaction and the percentage of photodegradation:

No. of cycles	Reaction rate $K \times 10^3\ (min^{-1})$	Photo degradation % at 180 min.
1st cycle	12.2	97.7
2nd cycle	11.4	97
3rd cycle	10.2	96.4
4th cycle	8.6	92.6
5th cycle	5.6	79.7

4- Conclusions

In this study the nanoarchitecture rGO-Mn_3O_4 was prepared hydrothermally and was succssfully confirmed. Among the photocatalytic study rGO-Mn_3O_4 has shown higher photocatalytic efficiency than pure Mn_3O_4 under visible light illumination without any oxidants; while rGO shown complete adsorption of MB in dark. The reaction rate constant of photo degradation for MB was 1.22×10^{-2} min^{-1} at catalyst load 1 $g.L^{-1}$ for 240 min. This goes in a parallel way with the high BET surface area (185.9 $m^2.g$) and pore diameter (7.2 Å) as well as lower gap energy of rGO-M (1.92 eV). The oxidation mechanism involves a limited role played by $^.O_2^-$ and $^.OH$, while an appreciable role played by both electrons (e^-) and positive holes (h+) in the MB oxidation mechanism. The rGO-Mn_3O_4 photocatalyst showed maximum efficiency for degrading MB in pH 11and high stability after 3 cycles with a decrease of about 1.3 % from its initial efficiency.

References:

[1] Geim, A. K., Graphene : Status and Prospects, *Science*, *1530* (2014), 1530–1534.

[2] Geim, A.K., Novoselov, K.S., The Rise of Graphene, *Nature Mater*, *6* (2007), 1–14.

[3] Castro Neto, A.H., Guinea,F., Peres, N.M.R., Novoselov, K.S., Geim, A.K., The electronic properties of graphene, *Rev. Mod. Phys.,* 81 (2009), 109 .

[4] Acik, M., Lee, G., Mattevi, C., Pirkle, A., Wallace, R. M., Chhowalla, M., Cho, M., Chabal, Y., The role of oxygen during thermal reduction of graphene oxide studied by infrared absorption spectroscopy. *Journal of Physical Chemistry C*, *115* (2011), 19761–19781.

[5] Lightcap, I. V., Kosel, T. H., & Kamat, P. V., Anchoring semiconductor and metal nanoparticles on a two-dimensional catalyst mat. storing and shuttling electrons with reduced graphene oxide. *Nano Letters*, *10* (2010), 577–583.

[6] Chandra, V., Park, J., Chun, Y., Lee, J. W., Hwang, I., & Kim, K. S., Water-Dispersible Magnetite-Reduced Graphene Oxide Composites for Arsenic Removal, *ACS Nano*, *4* (2010), 3979–3986.

[7] Shen, Y., Fang, Q., & Chen, B., Environmental applications of three-dimensional graphene-based macrostructures: adsorption, transformation, and detection., *Environmental Science and Technology*, *49* (2015), 67–84.

[8] Xu, H., Qu, Z., Zong, C., Huang, W., Quan, F., & Yan, N., MnO_x/Graphene for the Catalytic Oxidation and Adsorption of Elemental Mercury, *Environmental Science and Technology*, *49* (2015), 6823–6830.

[9] Wang, G., Feng, W., Zeng, X., Wang, Z., Feng, C., McCarthy, D. T., Deletic, A., Zhang, X., Highly recoverable TiO_2-GO nanocomposites for stormwater disinfection, *Water Research*, *94 (2016)*, 363–370.

[10] Liu, W., Ma, J., Shen, C., Wen, Y., & Liu, W., A pH-responsive and magnetically separable dynamic system for efficient removal of highly dilute antibiotics in water. *Water Research*, *90 (2016)*, 24–33.

[11] López Guerra, E., Shanmugharaj, A. M., Choi, W. S., & Ryu, S. H., Thermally reduced graphene oxide-supported nickel catalyst for hydrogen production by propane steam reforming. *Applied Catalysis A: General*, *468 (2013)*, 467–474.

[12] Lee, J. W., Hall, A., Kim, J., & Mallouk, T., A Facile and Template-Free Hydrothermal Synthesis of Mn_3O_4 Nanorods on Graphene Sheets for Advanced Supercapacitor Electrodes with Long Cycle Stability. Chemistry of Materials, 24 (2012), 1158–1164.

[13] Lee, D. W., V, L. D. L. S., Seo, J. W., Felix, L. L., Bustamante, A. D., Cole, J. M., & Barnes, C. H. W., The Structure of Graphite Oxide Investigation of Its Surface Chemical Groups, *Journal of Physical Chemistry C*, *114 (2010)*, 5723–5728.

[14] Viinikanoja, A., Kauppila, J., Damlin, P., Suominen, M., & Kvarnström, C., In situ FTIR and Raman spectroelectrochemical characterization of graphene oxide upon electrochemical reduction in organic solvents, *Physical Chemistry Chemical Physics*, *17* (2015), 12115–12123.

[15] Wang, X., Wang, W., Liu, Y., Ren, M., Xiao, H., & Liu, X., Characterization of Conformation and Locations of C-F Bonds in Graphene Derivative by Polarized ATR-FTIR, *Analytical Chemistry*, *88* (2016), 3926–3934.

[16] Ishii, M., Nakahira, M., & Yamanaka, T., Infrared Absorption Spectra And Cation Distributions In (Mn, Fe)$_3O_4$. *Solid State Communications*, 11 (1972), 209–212.

[17] Wang W. Z., Xu C. K., Wang G. H., Liu Y. K., & Zheng C. L., Synthesis and Characterization of Cu_2O Nanowires by a Novel Reduction Route, *Advanced Materials,* 14 (2002), 67–69.

[18] Gupta, N., Verma, A., Kashyap, S. C., & Dube, D. C., Microstructural, dielectric and magnetic behavior of spin-deposited nanocrystalline nickel-zinc ferrite thin films for microwave applications, *Journal of Magnetism and Magnetic Materials*, *308* (2007), 137–142.

[19] Lanfredi, S., Saia, S., Lebullenger, R., & Hernandes, C., Electric conductivity and relaxation in fluoride, fluorophosphate and phosphate glasses: Analysis by impedance spectroscopy. *Solid State Ionics*, *146* (2002), 329–339.

[20] Singh, V., Joung, D., Zhai, L., Das, S., Khondaker, I., & Seal, S., Graphene based materials: Past, present and future. *Progress in Materials Science*, *56* (2011), 1178–1271.

[21] Brunauer, S., Deming, S., Deming, E., & Teller, E., On a Theory of the van der Waals Adsorption of Gases, *J. Am. Chem. Soc.*, *62* (1940), 1723–1732.

[22] Sing, W., Everett, H., Haul, W., Moscou, L., Pierotti, A., Rouquerol, J., & Siemieniewska, T., Reporting physisorption data for gas/soils systems with special reference to the determination of surface area and porosity. *Pure Appl. Chemistry*, *57* (1985), 603–619.

[23] Rouquerol, J., Avnir, D., Fairbridge, W., Everett, H., Haynes, M., Pernicone, N., Ramsay, J., Sing, K., & Unger, K., Recommendations for the characterization of porous solids. *Pure and Applied Chemistry*, *66* (1994), 1739–1758.

[24] Chien, C. T., Li, S. S., Lai, W. J., Yeh, Y. C., Chen, H. A., Chen, I. S., Chen, L., Chen, K., Nemoto, T., Isoda, S., Chen, M., Fujita, T., Eda, G., Yamaguchi, H., Chhowalla, M., & Chen, W., Tunable photoluminescence from graphene oxide, *Angewandte Chemie - International Edition*, *51* (2012), 6662–6666.

[25] Toufiq, A. M., Wang, F., Javed, Q. U. A., Li, Q., & Li, Y., Hydrothermal synthesis of MnO_2 nanowires: Structural characterizations, optical and magnetic properties, *Applied Physics A: Materials Science and Processing*, *116* (2014), 1127–1132.

[26] Giri, A., Goswami, N., Pal, M., Zar Myint, M. T., Al-Harthi, S., Singha, A., Ghosh, B., Dutta, J., & Pal, S. K., Rational surface modification of Mn_3O_4 nanoparticles to induce multiple photoluminescence and room temperature ferromagnetism, *Materials Letters*, 118 (2013), 34–38.

[27] P. Kubelka and F. Munk, Ein Beitrag Zur Optik Der Farbanstriche, *Z. Tech. Phys*., 12 (1931), 593–599.

[28] Mandelis, A., & Grossman, J. P., Perturbation Theoretical Approach to the Generalized Kubelka-Munk Problem in Nonhomogeneous Optical Media, *Applied Spectroscopy*, *46* (1992), 737–745.

[29] Touc, J., Grigorovi, R., & Vancu, A., Optical Properties and Electronic Structure of Amorphous Germanium, *Physica Status Solidi (B)*, *15* (1966), 627–637.

[30] Peng, T., Xu, L., & Chen, H., Preparation and characterization of high specific surface area Mn_3O_4 from electrolytic manganese residue, *Central European Journal of Chemistry*, *8* (2010), 1059–1068.

[31] Low, J., Yu, J., Li, Q., & Cheng, B., Enhanced visible-light photocatalytic activity of plasmonic Ag and graphene co-modified Bi_2WO_6 nanosheets, *Physical Chemistry Chemical Physics*, *16* (2014), 1111–1120. ,

[32] Boruah, P. K., Borthakur, P., Darabdhara, G., Kamaja, C. K., Karbhal, I., Shelke, M. V., Phukan, P., Saikia, D., & Das, M. R., Sunlight assisted degradation of dye molecules and reduction of toxic Cr(VI) in aqueous medium using magnetically recoverable Fe_3O_4/reduced graphene oxide nanocomposite, *RSC Advances*, *6* (2016), 11049–11063. ,

[33] Calandra, P., Longo, A., Marciano, V., & Liveri, T., Physicochemical Investigation of Lightfast AgCl and AgBr Nanoparticles Synthesized by a Novel Solid - Solid Reaction. *J. Phys. Chem. B*, *107 (2003)*, 6724–6729.

[34] Beranek, R., (Photo)electrochemical methods for the determination of the band edge positions of TiO_2-based nanomaterials. *Advances in Physical Chemistry*, *2011* (2011), 80–83.